Coupling of MoS_2 Excitons with Lattice Phonons and Cavity Vibrational Phonons in Hybrid Nanobeam Cavities

Chenjiang Qian,[1,*] Viviana Villafañe,[1] Marko M. Petrić,[2] Pedro Soubelet,[1] Andreas V. Stier,[1] and Jonathan J. Finley[1,†]
[1]*Walter Schottky Institut and Physik Department, Technische Universität München, Am Coulombwall 4, 85748 Garching, Germany*
[2]*Walter Schottky Institut and Department of Electrical and Computer Engineering, Technische Universität München, Am Coulombwall 4, 85748 Garching, Germany*

(Received 3 June 2022; revised 23 January 2023; accepted 28 February 2023; published 23 March 2023)

We report resonant Raman spectroscopy of neutral excitons X^0 and intravalley trions X^- in hBN-encapsulated MoS_2 monolayer embedded in a nanobeam cavity. By temperature tuning the detuning between Raman modes of MoS_2 lattice phonons and X^0/X^- emission peaks, we probe the mutual coupling of excitons, lattice phonons and cavity vibrational phonons. We observe an enhancement of X^0-induced Raman scattering and a suppression for X^--induced, and explain our findings as arising from the tripartite exciton-phonon-phonon coupling. The cavity vibrational phonons provide intermediate replica states of X^0 for resonance conditions in the scattering of lattice phonons, thus enhancing the Raman intensity. In contrast, the tripartite coupling involving X^- is found to be much weaker, an observation explained by the geometry-dependent polarity of the electron and hole deformation potentials. Our results indicate that phononic hybridization between lattice and nanomechanical modes plays a key role in the excitonic photophysics and light-matter interaction in 2D-material nanophotonic systems.

DOI: 10.1103/PhysRevLett.130.126901

Nano-opto-electro-mechanical systems are of strong interest in the study of light-matter interactions since they intentionally couple electronic, optical, and vibrational degrees of freedom having vastly different eigenfrequencies [1–4]. Hereby, interband optical response becomes sensitive to the local optical field and the state of motion (phonons) in the nanosystem [5,6]. Monolayer transition metal dichalcogenides (TMDs) are of particular interest in this context since they (i) can be attached via van der Waals bonding to a wide range of different substrates, and they combine (ii) strong light-matter interactions through excitonic transitions at room temperature with (iii) large photoelastic coupling strengths to the local deformations [7–10]. Recent works on 2D-material nanophotonic cavities report that phonons modulate the light-matter interaction by limiting the exciton mobility [11] and introducing vibronic sublevels [12,13]. These phonon-mediated effects indicate wide potentials of phononic technology in the cavity QED study.

While these recent works spell out the key role played by phonons in 2D-material nanocavities [11–14], the additional degree of freedom associated with the phononic vibration from cavity nanomechanical modes and the delicate interplay between lattice phonons, nanomechanical modes, excitons, and cavity photons have not been previously elucidated. Indeed, besides the lattice phonons from atomic vibrational modes [15–18], there also exist the phononic vibrational modes of nanocavities [19–22]. The cavity vibrational phonons also introduce deformations and interact with excitons [23,24]. Therefore, understanding the interplay between different phonons and their mutual coupling to excitons are the key to further explore and control phonon-mediated processes in light-matter interactions.

In this Letter, we reveal the tripartite coupling between excitons, lattice phonons, and cavity vibrational phonons in the cavity-MoS_2 system using resonant Raman spectroscopy. We use optimized high-Q nanobeam cavities to embed hBN-encapsulated monolayer MoS_2 [11]. The encapsulation suppresses disorder-induced fluctuations [25–27] and allows clear spectral separation of *pristine* neutral excitons X^0 and intravalley trions X^-. We tune the Raman modes of MoS_2 lattice phonons through the exciton emission energies by the temperature [28]. The $X^0(X^-)$-phonon coupling strengths in the $X^0(X^-)$-induced Raman scattering are revealed by the X^0-Raman and X^--Raman resonant peaks in the detuning dependent Raman intensity [28–31]. We observe a significant enhancement of X^0-induced Raman scattering and a suppression for X^--induced. The enhancement of X^0-induced scattering is well explained by exciton-phonon-phonon coupling, where the cavity vibrational phonons provide intermediate replica states for resonance conditions in the scattering of lattice phonons. In contrast, the X^-–cavity-phonon coupling is very weak, explained by the near cancellation of electron and hole deformation potentials in the ribbon-shaped MoS_2 monolayers [32]. Thereby, the intermediate state that enhances the Raman intensity does not occur for

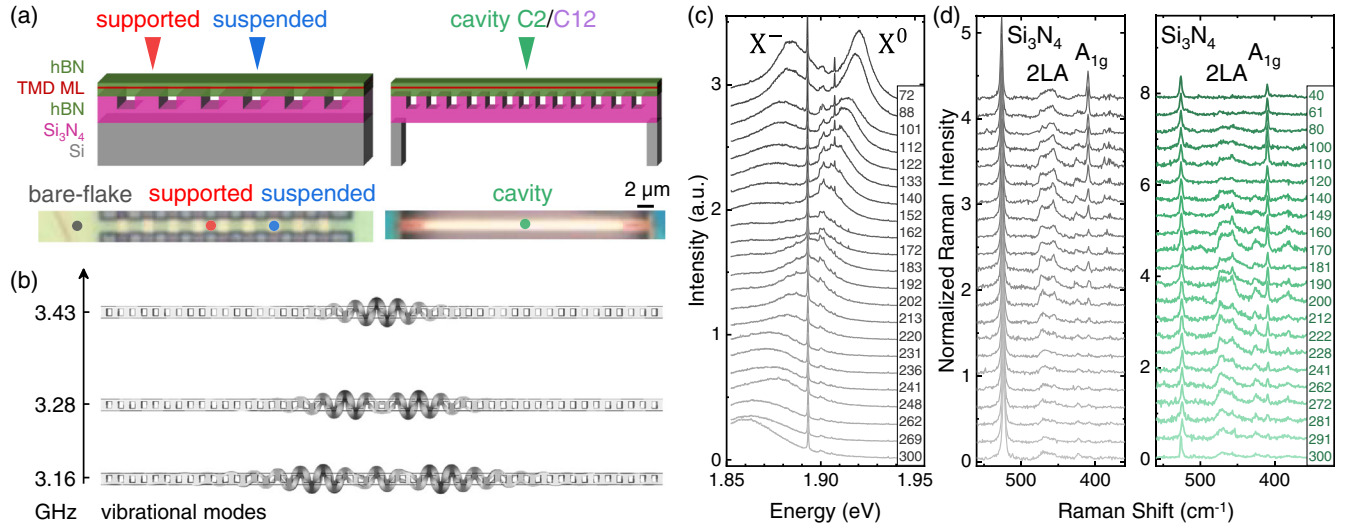

FIG. 1. (a) Schematic of four distinct laser positions for spectroscopy: bare flake off to the side of nanobeam on the planar substrate, supported on Si_3N_4 and suspended on etched Si_3N_4 part of the nanobeam, and the center position of the nanobeam cavity. (b) Calculated vibrational modes of the nanobeam cavity. The MoS_2 deforms primarily along the axis of nanobeam. (c) Temperature-dependent raw spectra recorded from the bare-flake showing both Raman and photoluminescence (PL) signals. (d) Raman spectra after subtracting the PL emission baseline recorded from the bare flake (gray) and cavity C2 (green). Intensities are normalized to the Si_3N_4 peak. Temperatures are denoted in Kelvin in the inset box in (c),(d).

X^-. The temperature dependence of Raman enhancement reveals that a discrete number of cavity phonons participate in the coupling, further supporting the phononic hybridization between material and nanomechanical degrees of freedom in the quantum system.

Our sample structures are depicted in Fig. 1(a). The hBN/MoS_2/hBN heterostructure is prepared using mechanical exfoliation and viscoelastic dry transfer methods [11,33]. The monolayer MoS_2 is encapsulated by the top (bottom) hBN with a thickness around 15 (55) nm, transferred onto a 200 nm thick Si_3N_4 layer on a Si substrate. The sample is patterned into series of photonic crystal nanobeams [11,34]. We investigate the Raman spectra recorded from four kinds of positions. The first case, bare flake, corresponds to the region consisting of only hBN-encapsulated MoS_2 on the planar Si_3N_4 substrate. Data recorded from this case are denoted by gray datasets in this work. The second and third cases, denoted by red and blue datasets, correspond to supported and suspended positions in the nanobeam, respectively. Since the photonic crystal trenches in this sample have a periodicity of 2 μm and a lateral size of 1 μm, the laser spot can be precisely and readily positioned on the supported or suspended positions, respectively. These three cases (bare flake, supported, suspended) are control experiments, in contrast to the fourth case cavity corresponding to the center position of high-Q cavities. In this work, we present data recorded from two cavities with the different nanobeam width 520 (420) nm for cavity C2 (C12). The data recorded from cavity C2 (C12) is denoted by green (purple) datasets, respectively. Optical and vibrational modes of the cavity are formed by chirping the photonic crystal periodicity to create photonic and phononic band gap confinement [11,20]. Typical vibrational modes calculated via fully 3D finite element simulation are presented in Fig. 1(b), and the calculation details are presented in Sec. II in the Supplemental Material [35].

The three control experiments, i.e., bare flake, supported and suspended cases are chosen to identify other factors besides the optical and vibrational modes which might affect the Raman properties in the cavity. For example, in the cavity two types of local static strain are induced in the TMD: tensile strain from Si_3N_4 structures [49,50] and strain arising from the 2D heterostructure being freely suspended. Effects from the former can be isolated by the supported case, and effects from the latter can be revealed by the suspended case. The reactive ion etching during nanofabrication might also affect the hBN/TMD/hBN heterostructure [51,52], and if this is the case, the effect on Raman properties can be revealed by both supported and suspended cases.

We implement resonant Raman spectroscopy by varying the lattice temperature to tune the Raman modes of MoS_2 lattice phonons through the X^0 and X^- emission. The excitation cw-laser laser has the wavelength 632 nm with a spot size ~1 μm and power ~100 μW. The excitation conditions produce both exciton emissions and Raman signals superimposed in spectra, as shown in the raw spectra measured from the bare flake in Fig. 1(c). Raman spectra are then extracted by subtracting the emission baseline, and the results from the bare flake and cavity C2 are presented in Fig. 1(d). We observe three dominant Raman modes: the Si_3N_4 phonon (525 cm^{-1}) and two MoS_2 lattice phonons as acoustic phonon 2LA

(450–480 cm^{-1}) and optical phonon A_{1g} (409 cm^{-1}) [53,54]. The intensity of 2LA peak in both cases exhibits a clear maximum around the resonance to X^0, which is a typical resonant Raman phenomenon [28–30]. Meanwhile, differences are observed between cavities and control experiments, e.g., the intensity of 2LA peak at low temperature, indicating the phonons and exciton-phonon couplings are modulated in the cavity.

To further investigate the exciton-phonon couplings, we normalize the Raman intensities by dividing the integrated peak intensity by the Bose factor and the intensity of Si_3N_4 peak [10], i.e.,

$$I'_{A_{1g}} = \frac{I_{A_{1g}}/(n_{A_{1g}}+1)}{I_{SiN}/(n_{SiN}+1)}, \qquad I'_{2LA} = \frac{I_{2LA}/(n_{LA}+1)^2}{I_{SiN}/(n_{SiN}+1)},$$

where $I_{A_{1g}}$, I_{SiN}, and I_{2LA} are peak intensities extracted from Raman spectra. $n_{A_{1g}}$, n_{SiN}, n_{LA} are temperature-dependent Bose distribution factors

$$n_p = \frac{1}{e^{\hbar(\omega_{Laser}-\omega_p)/(k_B T)}-1}, \qquad p = \{A_{1g}, 2LA, SiN\},$$

where $\hbar\omega_{Laser}$ ($\hbar\omega_p$) is the energy of the laser (Raman mode), k_B is the Boltzmann constant, and T is the temperature. Theoretically, the normalized Raman intensity consists of signals from all possible light-matter intermediate states, according to [55]

$$\sum_m \left| \frac{M_{fm} M_{ep} M_{mi}}{(\omega_m - (i/2)\gamma_m - \omega_{Laser})(\omega_m - (i/2)\gamma_m - \omega_p)} \right|^2,$$

where i, m, and f denote the initial, intermediate, and final states, ω_m and γ_m are the energy and lifetime of the intermediate state m, M_{fm} (M_{mi}) is the matrix element of the optical $f \leftarrow m$ ($m \leftarrow i$) transition, and M_{ep} is the matrix element quantifying the exciton-phonon coupling strength. In our measurements, X^0 and X^- are near resonant to the outgoing Raman modes. Thus, the exciton-Raman detuning (outgoing Raman resonance) dominates the detuning-dependent Raman intensities. We thereby fit the normalized Raman intensities using

$$I'_p = \sum_X g_{X,p} R_{X,p}, \qquad X = \{X^0, X^-\},$$
$$p = \{A_{1g}, 2LA\} \qquad R_{X,p} = 1/|\omega_X - (i/2)\gamma_X - \omega_p|^2,$$

where $g_{X,p}$ reflects the exciton-phonon coupling strength and $R_{X,p}$ is the exciton-Raman detuning modeled by Fermi's golden rule [28,30,31]. The Raman mode energy ω_p are extracted from the Raman spectra. Since the exciton-Raman resonance deforms the exciton emission line shape [29,56], we extract the exciton energy ω_X and linewidth γ_X from the PL spectra excited by 532 nm-laser (off resonance, see Sec. IV A in the Supplemental Material [35]).

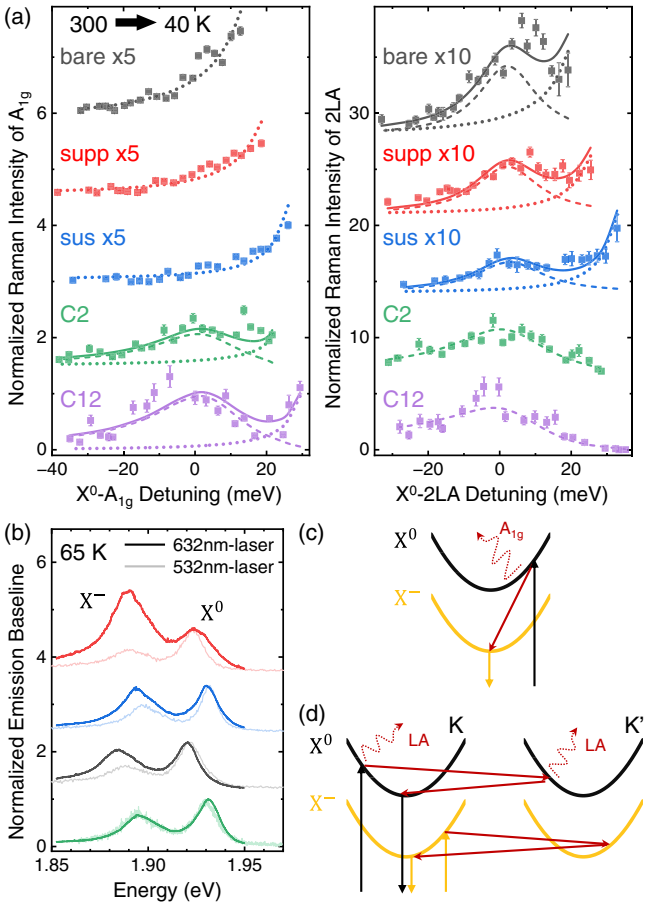

FIG. 2. (a) Normalized Raman intensities of A_{1g} and 2LA. Dashed (dotted) peaks are from the $X^0(X^-)$-phonon coupling. In control cases (gray, red, blue) the coupling strength $g_{X,p}$ is constant. In cavities (green, purple), $g_{X^-,p}$ is constant and $g_{X^0,p}$ is enhanced with a T^N dependence. (b) Comparisons between exciton emission recorded using 632 nm-laser (dark) and 532 nm-laser (light) at 65 K, normalized by the X^0 peak. (c) Schematic of doubly resonant scattering of A_{1g} around X^--Raman resonance, which converts X^0 to X^-, thereby enhances the X^- emission in (b) for the three control cases. (d) Schematic of the doubly resonant scattering of 2LA around $X^0(X^-)$-Raman resonance.

The results of A_{1g} and 2LA measured from the three control cases and two cavities are plotted in Fig. 2(a) as a function of the energy detuning to X^0. Dashed lines represent the resonance arising from the coupling to X^0, and dotted lines represent the expected resonance arising from the coupling to X^-, ~35 meV detuned from X^0 [29]. In three control cases (gray, red, blue), the coupling strength $g_{X,p}$ is nearly constant [28,30,31]. The results reveal that for A_{1g}, only $g_{X^-,A1g}$ has a significant amplitude whilst $g_{X^0,A1g}$ vanishes. For 2LA both $g_{X^0,2LA}$ and $g_{X^-,2LA}$ have finite amplitudes. Another distinctive feature of

X^--Raman resonance is the enhanced ratio of X^-/X^0 emission intensity [29,56] as clearly observed in three control cases presented in Fig. 2(b), where exciton emission around 65 K recorded using the 632 nm-laser (dark, close to X^--Raman resonance) are compared with those using the 532 nm-laser (light, off-resonance). This is due to the doubly resonant Raman scattering depicted in Fig. 2(c), where X^0 is converted to X^- by the phonon scattering [56–58]. In contrast to the three control cases, Raman spectra recorded from the cavities exhibit entirely different behaviors that are traced to cavity vibrational phonons. As shown in Fig. 2(a), $g_{X^0,A1g}$ is clearly nonzero in two cavities, evidenced by the resonance (dashed peak) which is in contrast absent in the three control cases. Meanwhile, $g_{X^0,2LA}$ (dashed peak) is enhanced in cavities while the amplitude of $g_{X^-,2LA}$ (dotted peak) vanishes. Therefore, we conclude that X^0-phonon coupling strengths are enhanced in cavities while X^--phonon coupling strengths are suppressed. The suppression of $g_{X^-,p}$ is also supported by the exciton emission presented in Fig. 2(b). The X^- emission enhancement [29] arising from X^--Raman resonance [Fig. 2(c)] is not observed in the cavity.

We note that ingoing Raman resonances have little impact on the measured intensities, since the laser is far detuned from both exciton peaks (X^0-laser resonance corresponds to 60 meV in X^0-Raman detuning). Moreover, here A_{1g} and 2LA contain doubly resonant Raman scatterings [30,31,56], thereby, the ingoing excitation is not limited to the zone center, as depicted schematically in Figs. 2(c) and 2(d). For the ideal first-order Raman scattering, the ingoing excitation is limited at the zone center, thereby the ingoing resonance between ω_{Laser} and ω_{X^0} play a role in the variation of the Raman intensity. In contrast, in our measurements around the exciton-Raman resonance depicted in Figs. 2(c) and 2(d), only the outgoing section is around the zone center, thereby the outgoing resonances $R_{X,p}$ are expected to dominate the spectral dependencies. Therefore, we fit the detuning-dependent Raman intensities by $R_{X,p}$ as presented in Fig. 2(a). Nevertheless, at this point we emphasize that the conclusions above can be directly obtained from raw data, without making this approximation and quantitative fittings as discussed in Sec. III A in the Supplemental Material [35].

Furthermore, the cavity enhanced coupling strengths $g_{X^0,A_{1g}}$ and $g_{X^0,2LA}$ are found to follow a temperature-dependent power law T^N. This can be seen in Fig. 3(a) that shows $g_{X^0,2LA} = I'_{2LA}/R_{X^0,2LA}$ from which we extract $N = 1.14 \pm 0.18$ and 2.21 ± 0.23 for cavity C2 and C12, respectively. The selective enhancement of $g_{X^0,p}$ ($p = \{A_{1g}, 2LA\}$), and the T^N dependence are two key observations in this work, indicating the tripartite coupling between excitons, cavity vibrational phonons and MoS_2 lattice phonons. This exciton-phonon-phonon coupling we envisage is illustrated schematically in Fig. 3(b): cavity

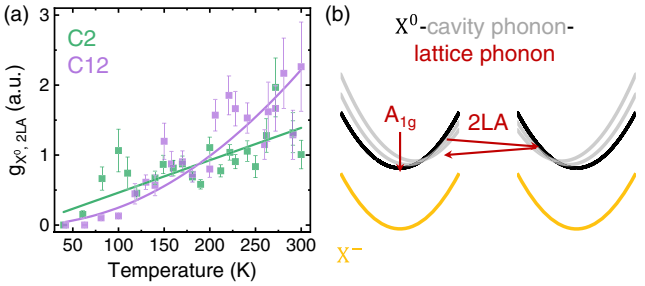

FIG. 3. (a) T^N dependence of $g_{X^0,2LA}$ in cavities. (b) Schematic depiction of the exciton-phonon-phonon coupling between X^0 (black), cavity phonon (gray replicas), and lattice phonons (dark red arrows).

vibrational phonons provide additional intermediate states indicated by the gray replicas that can satisfy the resonance conditions in the scattering of MoS_2 lattice phonons (dark red arrows). The selectivity is due to the vibronic states (gray replicas) that only occur for X^0 but not for X^-. We explain this suggest by the weak X^-–cavity-phonon coupling originating from the geometry-dependent deformation potentials. In cavity vibrational modes, the embedded ribbon-shaped MoS_2 monolayer extends primarily along the nanobeam axis. For such uniaxially strained MoS_2, Cai *et al.* [32] calculated the width dependent deformation potential for the electrons (D_e) and holes (D_h). D_h was always found to have a magnitude that is approximately twice of D_e [32]. Therefore, the X^-–cavity-phonon coupling strength ($\propto 2D_e - D_h$) is expected to be much smaller than the X^0–cavity-phonon coupling strength ($\propto D_e - D_h$) [59–61]. This selectivity is further supported by the temperature-dependent linewidth of excitonic PL emission, discussed in SFig. 14 in the Supplemental Material [35].

Meanwhile, the T^N dependence is consistent with the Bose occupation of cavity vibrational phonons $n_{cP} = 1/[e^{\hbar\omega_{cP}/(k_B T)} - 1]$. Since the cavity vibrational phonon has low energy [Fig. 1(b)] $\hbar\omega_{cP} \ll k_B T$, the temperature dependent factor of either Stokes ($n_{cP}+1$) or anti-Stokes (n_{cP}) processes is $\approx k_B T/(\hbar\omega_{cP}) \propto T$. Thereby, N is determined by the number of cavity phonons participating in the tripartite coupling. Additional evidence for the tripartite coupling is observed from the spatial dependence of Raman enhancement and the temperature dependence of Raman linewidth (anharmonicity) [62] as discussed in Sec. III B in the Supplemental Material [35]. Similar vibronic sublevel mediated processes have been reported in photonic [12–14,63] and plasmonic systems [64,65]. In contrast, other factors do not explain the experimental results. For example, the control experiments in the supported and suspended case show that both two types of static strain without cavity vibrational modes do not result in the selective Raman enhancement. Indeed, the static strain is not proportional to temperature, and thereby, it cannot explain the T^N

dependence. The resonant cavity optical mode could of course enhance the Raman intensity by increasing the local optical field for the laser [66,67] or exciton spontaneous emissions [64,67,68]. However, these effects are strongly dependent on the detuning of the cavity optical mode to the laser or excitonic transitions. In our experiments, the excitation laser and Raman modes are far detuned from the cavity optical mode (> 20 meV), and the detuning is nearly temperature independent. The coupling between X^0 and the cavity optical mode is negligible [11], and no dependence on their detuning is observed in Fig. 3(a). Therefore, several pieces of evidence all indicate that the cavity optical mode does not play the major role in determining the observed Raman enhancement.

In summary, we performed spatially resolved Raman spectroscopy to demonstrate how excitons, MoS_2 lattice phonons and cavity vibrational phonons couple to govern the exciton-phonon scattering in 2D-material nanophotonic cavities. The selectivity to the neutral exciton indicates such phononic technology can be applied to control light-matter interactions based on different electronic transitions (excitonic sorting). Moreover, our results are obtained for thermally excited vibrational modes without external driving [22,23]. Therefore, our results indicate that the phononic hybridization between lattice and nanomechanical modes has an intrinsic strong impact on excitonic photophysics and light-matter interactions in 2D-material nanophotonic systems.

All authors gratefully acknowledge the German Science Foundation (DFG) for financial support via Grants No. FI 947/8-1, No. DI 2013/5-1, and No. SPP-2244, as well as the clusters of excellence MCQST (EXS-2111) and e-conversion (EXS-2089). C. Q. and V. V. gratefully acknowledge the Alexander v. Humboldt Foundation for financial support in the framework of their fellowship program.

C. Q. and V. V. contributed equally to this work.

*chenjiang.qian@wsi.tum.de
†finley@wsi.tum.de

[1] I. Mahboob, K. Nishiguchi, H. Okamoto, and H. Yamaguchi, Phonon-cavity electromechanics, Nat. Phys. **8**, 387 (2012).
[2] M. Aspelmeyer, T. J. Kippenberg, and F. Marquardt, Cavity optomechanics, Rev. Mod. Phys. **86**, 1391 (2014).
[3] K. E. Khosla, M. R. Vanner, N. Ares, and E. A. Laird, Displacemon Electromechanics: How to Detect Quantum Interference in a Nanomechanical Resonator, Phys. Rev. X **8**, 021052 (2018).
[4] L. Midolo, A. Schliesser, and A. Fiore, Nano-opto-electro-mechanical systems, Nat. Nanotechnol. **13**, 11 (2018).
[5] Y.-C. Wei, S. F. Wang, Y. Hu, L.-S. Liao, D.-G. Chen, K.-H. Chang, C.-W. Wang, S.-H. Liu, W.-H. Chan, J.-L. Liao, W.-Y. Hung, T.-H. Wang, P.-T. Chen, H.-F. Hsu, Y. Chi, and P.-T. Chou, Overcoming the energy gap law in near-infrared OLEDs by exciton–vibration decoupling, Nat. Photonics **14**, 570 (2020).
[6] T. Zhang, H. Wang, X. Xia, N. Yan, X. Sha, J. Huang, K. Watanabe, T. Taniguchi, M. Zhu, L. Wang, J. Gao, X. Liang, C. Qin, L. Xiao, D. Sun, J. Zhang, Z. Han, and X. Li, A monolithically sculpted van der Waals nano-opto-electro-mechanical coupler, Light Sci Appl. **11**, 48 (2022).
[7] M. Ghorbani-Asl, N. Zibouche, M. Wahiduzzaman, A. F. Oliveira, A. Kuc, and T. Heine, Electromechanics in MoS2 and WS2: Nanotubes vs. monolayers, Sci. Rep. **3**, 2961 (2013).
[8] B. Miller, J. Lindlau, M. Bommert, A. Neumann, H. Yamaguchi, A. Holleitner, A. Högele, and U. Wurstbauer, Tuning the Fröhlich exciton-phonon scattering in monolayer MoS2, Nat. Commun. **10**, 807 (2019).
[9] N. Morell, A. Reserbat-Plantey, I. Tsioutsios, K. G. Schädler, F. Dubin, F. H. L. Koppens, and A. Bachtold, High quality factor mechanical resonators based on WSe2 monolayers, Nano Lett. **16**, 5102 (2016).
[10] P. Soubelet, A. A. Reynoso, A. Fainstein, K. Nogajewski, M. Potemski, C. Faugeras, and A. E. Bruchhausen, The lifetime of interlayer breathing modes of few-layer 2H-MoSe2 membranes, Nanoscale **11**, 10446 (2019).
[11] C. Qian, V. Villafañe, P. Soubelet, A. Hötger, T. Taniguchi, K. Watanabe, N. P. Wilson, A. V. Stier, A. W. Holleitner, and J. J. Finley, Nonlocal Exciton-Photon Interactions in Hybrid High-Q Beam Nanocavities with Encapsulated MoS_2 Monolayers, Phys. Rev. Lett. **128**, 237403 (2022).
[12] S. Latini, U. De Giovannini, E. J. Sie, N. Gedik, H. Hübener, and A. Rubio, Phonoritons as Hybridized Exciton-Photon-Phonon Excitations in a Monolayer h-BN Optical Cavity, Phys. Rev. Lett. **126**, 227401 (2021).
[13] D. Li, H. Shan, C. Rupprecht, H. Knopf, K. Watanabe, T. Taniguchi, Y. Qin, S. Tongay, M. Nuß, S. Schröder, F. Eilenberger, S. Höfling, C. Schneider, and T. Brixner, Hybridized Exciton-Photon-Phonon States in a Transition Metal Dichalcogenide van der Waals Heterostructure Microcavity, Phys. Rev. Lett. **128**, 087401 (2022).
[14] D. Rosser, T. Fryett, A. Ryou, A. Saxena, and A. Majumdar, Exciton–phonon interactions in nanocavity-integrated monolayer transition metal dichalcogenides, npj 2D Mater. Appl. **4**, 20 (2020).
[15] M. Selig, G. Berghäuser, A. Raja, P. Nagler, C. Schüller, T. F. Heinz, T. Korn, A. Chernikov, E. Malic, and A. Knorr, Excitonic linewidth and coherence lifetime in monolayer transition metal dichalcogenides, Nat. Commun. **7**, 13279 (2016).
[16] P. Dey, J. Paul, Z. Wang, C. E. Stevens, C. Liu, A. H. Romero, J. Shan, D. J. Hilton, and D. Karaiskaj, Optical Coherence in Atomic-Monolayer Transition-Metal Dichalcogenides Limited by Electron-Phonon Interactions, Phys. Rev. Lett. **116**, 127402 (2016).
[17] M. Titze, B. Li, X. Zhang, P. M. Ajayan, and H. Li, Intrinsic coherence time of trions in monolayer $MoSe_2$ measured via two-dimensional coherent spectroscopy, Phys. Rev. Mater. **2**, 054001 (2018).
[18] G. Gupta and K. Majumdar, Fundamental exciton linewidth broadening in monolayer transition metal dichalcogenides, Phys. Rev. B **99**, 085412 (2019).

[19] M. Eichenfield, R. Camacho, J. Chan, K. J. Vahala, and O. Painter, A picogram- and nanometre-scale photonic-crystal optomechanical cavity, Nature (London) **459**, 550 (2009).
[20] M. Eichenfield, J. Chan, R. M. Camacho, K. J. Vahala, and O. Painter, Optomechanical crystals, Nature (London) **462**, 78 (2009).
[21] M. K. Zalalutdinov, J. T. Robinson, J. J. Fonseca, S. W. LaGasse, T. Pandey, L. R. Lindsay, T. L. Reinecke, D. M. Photiadis, J. C. Culbertson, C. D. Cress, and B. H. Houston, Acoustic cavities in 2D heterostructures, Nat. Commun. **12**, 3267 (2021).
[22] H. Xie, S. Jiang, D. A. Rhodes, J. C. Hone, J. Shan, and K. F. Mak, Tunable exciton-optomechanical coupling in suspended monolayer MoSe2, Nano Lett. **21**, 2538 (2021).
[23] M. Montinaro, G. Wüst, M. Munsch, Y. Fontana, E. Russo-Averchi, M. Heiss, A. Fontcuberta i Morral, R. J. Warburton, and M. Poggio, Quantum dot opto-mechanics in a fully self-assembled nanowire, Nano Lett. **14**, 4454 (2014).
[24] J. C. H. Chen, Y. Sato, R. Kosaka, M. Hashisaka, K. Muraki, and T. Fujisawa, Enhanced electron-phonon coupling for a semiconductor charge qubit in a surface phonon cavity, Sci. Rep. **5**, 15176 (2015).
[25] F. Cadiz, E. Courtade, C. Robert, G. Wang, Y. Shen, H. Cai, T. Taniguchi, K. Watanabe, H. Carrere, D. Lagarde, M. Manca, T. Amand, P. Renucci, S. Tongay, X. Marie, and B. Urbaszek, Excitonic Linewidth Approaching the Homogeneous Limit in MoS_2-Based van der Waals Heterostructures, Phys. Rev. X **7**, 021026 (2017).
[26] J. Wierzbowski, J. Klein, F. Sigger, C. Straubinger, M. Kremser, T. Taniguchi, K. Watanabe, U. Wurstbauer, A. W. Holleitner, M. Kaniber, K. Müller, and J. J. Finley, Direct exciton emission from atomically thin transition metal dichalcogenide heterostructures near the lifetime limit, Sci. Rep. **7**, 12383 (2017).
[27] A. Raja, L. Waldecker, J. Zipfel, Y. Cho, S. Brem, J. D. Ziegler, M. Kulig, T. Taniguchi, K. Watanabe, E. Malic, T. F. Heinz, T. C. Berkelbach, and A. Chernikov, Dielectric disorder in two-dimensional materials, Nat. Nanotechnol. **14**, 832 (2019).
[28] J.-H. Fan, P. Gao, A.-M. Zhang, B.-R. Zhu, H.-L. Zeng, X.-D. Cui, R. He, and Q.-M. Zhang, Resonance Raman scattering in bulk 2H-MX2 (M = Mo, W; X = S, Se) and monolayer MoS2, J. Appl. Phys. **115**, 053527 (2014).
[29] M. R. Molas, K. Nogajewski, M. Potemski, and A. Babiński, Raman scattering excitation spectroscopy of monolayer WS2, Sci. Rep. **7**, 5036 (2017).
[30] B. R. Carvalho, Y. Wang, S. Mignuzzi, D. Roy, M. Terrones, C. Fantini, V. H. Crespi, L. M. Malard, and M. A. Pimenta, Intervalley scattering by acoustic phonons in two-dimensional MoS2 revealed by double-resonance Raman spectroscopy, Nat. Commun. **8**, 14670 (2017).
[31] R. N. Gontijo, G. C. Resende, C. Fantini, and B. R. Carvalho, Double resonance Raman scattering process in 2D materials, J. Mater. Res. **34**, 1976 (2019).
[32] Y. Cai, G. Zhang, and Y.-W. Zhang, Polarity-reversed robust carrier mobility in monolayer MoS2 nanoribbons, J. Am. Chem. Soc. **136**, 6269 (2014).
[33] F. Pizzocchero, L. Gammelgaard, B. S. Jessen, J. M. Caridad, L. Wang, J. Hone, P. Bøggild, and T. J. Booth, The hot pick-up technique for batch assembly of van der Waals heterostructures, Nat. Commun. **7**, 11894 (2016).
[34] C. Qian, V. Villafañe, M. Schalk, G. V. Astakhov, U. Kentsch, M. Helm, P. Soubelet, N. P. Wilson, R. Rizzato, S. Mohr, A. W. Holleitner, D. B. Bucher, A. V. Stier, and J. J. Finley, Unveiling the zero-phonon line of the boron vacancy center by cavity-enhanced emission, Nano Lett. **22**, 5137 (2022).
[35] See Supplemental Material at http://link.aps.org/supplemental/10.1103/PhysRevLett.130.126901 for methods, additional Raman results, and supporting evidence from PL spectroscopy, which includes Refs. [36–48].
[36] Z. Huang, A. Alharbi, W. Mayer, E. Cuniberto, T. Taniguchi, K. Watanabe, J. Shabani, and D. Shahrjerdi, Versatile construction of van der Waals heterostructures using a dual-function polymeric film, Nat. Commun. **11**, 3029 (2020).
[37] M. He, P. Rivera, D. Van Tuan, N. P. Wilson, M. Yang, T. Taniguchi, K. Watanabe, J. Yan, D. G. Mandrus, H. Yu, H. Dery, W. Yao, and X. Xu, Valley phonons and exciton complexes in a monolayer semiconductor, Nat. Commun. **11**, 618 (2020).
[38] Y. Yu, J. Dang, C. Qian, S. Sun, K. Peng, X. Xie, S. Wu, F. Song, J. Yang, S. Xiao, L. Yang, Y. Wang, X. Shan, M. A. Rafiq, B.-B. Li, and X. Xu, Many-body effect of mesoscopic localized states in MoS_2 monolayer, Phys. Rev. Mater. **3**, 051001(R) (2019).
[39] J. Klein, M. Florian, A. Hötger, A. Steinhoff, A. Delhomme, T. Taniguchi, K. Watanabe, F. Jahnke, A. W. Holleitner, M. Potemski, C. Faugeras, A. V. Stier, and J. J. Finley, Trions in MoS_2 are quantum superpositions of intra- and intervalley spin states, Phys. Rev. B **105**, L041302 (2022).
[40] S. Thomas, K. M. Ajith, S. Chandra, and M. C. Valsakumar, Temperature dependent structural properties and bending rigidity of pristine and defective hexagonal boron nitride, J. Phys. Condens. Matter **27**, 315302 (2015).
[41] G. Berghäuser, P. Steinleitner, P. Merkl, R. Huber, A. Knorr, and E. Malic, Mapping of the dark exciton landscape in transition metal dichalcogenides, Phys. Rev. B **98**, 020301(R) (2018).
[42] J. Krustok, R. Kaupmees, R. Jaaniso, V. Kiisk, I. Sildos, B. Li, and Y. Gong, Local strain-induced band gap fluctuations and exciton localization in aged WS2 monolayers, AIP Adv. **7**, 065005 (2017).
[43] Y. Hu, F. Zhang, M. Titze, B. Deng, H. Li, and G. J. Cheng, Straining effects in MoS2 monolayer on nanostructured substrates: Temperature-dependent photoluminescence and exciton dynamics, Nanoscale **10**, 5717 (2018).
[44] Z. Khatibi, M. Feierabend, M. Selig, S. Brem, C. Linderälv, P. Erhart, and E. Malic, Impact of strain on the excitonic linewidth in transition metal dichalcogenides, 2D Mater. **6**, 015015 (2018).
[45] F. Song, C. Qian, Y. Wang, F. Zhang, K. Peng, S. Wu, X. Xie, J. Yang, S. Sun, Y. Yu, J. Dang, S. Xiao, L. Yang, K. Jin, H. Zhong, and X. Xu, Hot Polarons with trapped excitons and octahedra-twist phonons in CH3NH3PbBr3 hybrid perovskite nanowires, Laser Photonics Rev. **14**, 1900267 (2020).
[46] X. Du, G. Blugan, T. Künniger, S. S. Lee, L. Vladislavova, and S. J. Ferguson, Non-linear mechanical properties and

dynamic response of silicon nitride bioceramic, Ceram. Int. **47**, 33525 (2021).
[47] H. Mathieu, P. Merle, E. L. Ameziane, B. Archilla, J. Camassel, and G. Poiblaud, Deformation potentials of the direct and indirect absorption edges of GaP, Phys. Rev. B **19**, 2209 (1979).
[48] R. Singh, A. Sarkar, C. Guria, R. J. Nicholl, S. Chakraborty, K. I. Bolotin, and S. Ghosh, Giant tunable mechanical nonlinearity in graphene–silicon nitride hybrid resonator, Nano Lett. **20**, 4659 (2020).
[49] D. Hoch, X. Yao, and M. Poot, Geometric Tuning of stress in predisplaced silicon nitride resonators, Nano Lett. **22**, 4013 (2022).
[50] Y. Chai, S. Su, D. Yan, M. Ozkan, R. Lake, and C. S. Ozkan, Strain gated bilayer molybdenum disulfide field effect transistor with edge contacts, Sci. Rep. **7**, 41593 (2017).
[51] S. Kim, J. E. Fröch, J. Christian, M. Straw, J. Bishop, D. Totonjian, K. Watanabe, T. Taniguchi, M. Toth, and I. Aharonovich, Photonic crystal cavities from hexagonal boron nitride, Nat. Commun. **9**, 2623 (2018).
[52] J. E. Fröch, Y. Hwang, S. Kim, I. Aharonovich, and M. Toth, Photonic nanostructures from hexagonal boron nitride, Adv. Opt. Mater. **7**, 1801344 (2019).
[53] R. Saito, Y. Tatsumi, S. Huang, X. Ling, and M. S. Dresselhaus, Raman spectroscopy of transition metal dichalcogenides, J. Phys. Condens. Matter **28**, 353002 (2016).
[54] A. Molina-Sánchez and L. Wirtz, Phonons in single-layer and few-layer MoS_2 and WS_2, Phys. Rev. B **84**, 155413 (2011).
[55] A. Jorio, R. Saito, G. Dresselhaus, and M. S. Dresselhaus, Quantum description of Raman scattering, in *Raman Spectroscopy in Graphene Related Systems* (John Wiley & Sons, Ltd, New York, 2011), Chap. 5, pp. 103–119, 10.1002/9783527632695.ch5.
[56] A. M. Jones, H. Yu, J. R. Schaibley, J. Yan, D. G. Mandrus, T. Taniguchi, K. Watanabe, H. Dery, W. Yao, and X. Xu, Excitonic luminescence upconversion in a two-dimensional semiconductor, Nat. Phys. **12**, 323 (2016).
[57] D. Van Tuan, A. M. Jones, M. Yang, X. Xu, and H. Dery, Virtual Trions in the Photoluminescence of Monolayer Transition-Metal Dichalcogenides, Phys. Rev. Lett. **122**, 217401 (2019).
[58] S. Ayari, S. Jaziri, R. Ferreira, and G. Bastard, Phonon-assisted exciton/trion conversion efficiency in transition metal dichalcogenides, Phys. Rev. B **102**, 125410 (2020).
[59] S. Helmrich, A. W. Achtstein, H. Ahmad, M. Kunz, B. Herzog, O. Schoeps, U. Woggon, and N. Owschimikow, noop High phonon-limited mobility of charged and neutral excitons in mono- and bilayer MoTe2, arXiv:2004.14202.
[60] L. Besombes, K. Kheng, L. Marsal, and H. Mariette, Acoustic phonon broadening mechanism in single quantum dot emission, Phys. Rev. B **63**, 155307 (2001).
[61] M. T. Portella-Oberli, J. Berney, L. Kappei, F. Morier-Genoud, J. Szczytko, and B. Deveaud-Plédran, Dynamics of Trion Formation in $In_xGa_{1-x}As$ Quantum Wells, Phys. Rev. Lett. **102**, 096402 (2009).
[62] H.-N. Liu, X. Cong, M.-L. Lin, and P.-H. Tan, The intrinsic temperature-dependent Raman spectra of graphite in the temperature range from 4 K to 1000 K, Carbon **152**, 451 (2019).
[63] A. Rundquist, A. Majumdar, and J. Vučković, Off-resonant coupling between a single quantum dot and a nanobeam photonic crystal cavity, Appl. Phys. Lett. **99**, 251907 (2011).
[64] T. c. v. Neuman, R. Esteban, G. Giedke, M. K. Schmidt, and J. Aizpurua, Quantum description of surface-enhanced resonant Raman scattering within a hybrid-optomechanical model, Phys. Rev. A **100**, 043422 (2019).
[65] E. C. Le Ru and P. G. Etchegoin, Vibrational pumping and heating under SERS conditions: Fact or myth?, Faraday Discuss. **132**, 63 (2006).
[66] R. Salter, J. Chu, and M. Hippler, Cavity-enhanced Raman spectroscopy with optical feedback cw diode lasers for gas phase analysis and spectroscopy, Analyst **137**, 4669 (2012).
[67] P. Wang, W. Chen, F. Wan, J. Wang, and J. Hu, A review of cavity-enhanced Raman spectroscopy as a gas sensing method, Appl. Spectrosc. Rev. **55**, 393 (2020).
[68] I. Irfan, S. Golovynskyi, M. Bosi, L. Seravalli, O. A. Yeshchenko, B. Xue, D. Dong, Y. Lin, R. Qiu, B. Li, and J. Qu, Enhancement of Raman scattering and exciton/trion photoluminescence of monolayer and few-layer MoS2 by Ag nanoprisms and nanoparticles: Shape and size effects, J. Phys. Chem. C **125**, 4119 (2021).